

# Transient Fragments in Outbursting Comet 17P/Holmes <sup>1,2</sup>

Rachel Stevenson

Dept. Earth and Space Sciences, UCLA

595 Charles Young Drive East, Los Angeles, CA 90095-1567

`stevenson@ucla.edu`

Jan Kleya

Institute for Astronomy, University of Hawaii

2680 Woodlawn Drive, Honolulu, HI 96822

`kleya@ifa.hawaii.edu`

and

David Jewitt

Dept. Earth and Space Sciences, Institute for Geophysics and Planetary Physics, UCLA

595 Charles Young Drive East, Los Angeles, CA 90095-1567

`jewitt@ucla.edu`

Received \_\_\_\_\_; accepted \_\_\_\_\_

## ABSTRACT

We present results from a wide-field imaging campaign at the Canada-France-Hawaii Telescope to study the spectacular outburst of comet 17P/Holmes in late 2007. Using image-processing techniques we probe inside the spherical dust coma and find sixteen fragments having both spatial distribution and kinematics consistent with isotropic ejection from the nucleus. Photometry of the fragments is inconsistent with scattering from monolithic, inert bodies. Instead, each detected fragment appears to be an active cometsimal producing its own dust coma. By scaling from the coma of the primary nucleus of 17P/Holmes, assumed to be 1.7 km in radius, we infer that the sixteen fragments have maximum effective radii between  $\sim 10$  m and  $\sim 100$  m on UT 2007 Nov. 6. The fragments subsequently fade at a common rate of  $\sim 0.2$  mag day $^{-1}$ , consistent with steady depletion of ices from these bodies in the heat of the Sun. Our characterization of the fragments supports the hypothesis that a large piece of material broke away from the nucleus and crumbled, expelling smaller, icy shards into the larger dust coma around the nucleus.

*Subject headings:* comets: individual (17P/Holmes)

## 1. Introduction

Comet 17P/Holmes is a dynamically and compositionally typical Jupiter Family Comet (Schleicher 2009) but it has exhibited three dramatic outbursts that caused an increase in brightness large enough to lift it from obscurity to naked-eye visibility (Holmes 1892; Palisa 1893; Buzzi et al. 2007). The first outburst led to its discovery on UT 1892 Nov. 6 by Edwin Holmes (Holmes 1892) and was followed by a second outburst three months later in January 1893. The third outburst, first identified by J. A. Henriquez Santana on UT 2007 Oct. 24 (Buzzi et al. 2007), caused the comet to reach a brightness of  $2^{nd}$  magnitude.

The nature of cometary mass loss varies widely between comets, ranging from gentle outgassing to violent outbursts as observed in the case of 17P/Holmes. Possible causes of large outbursts are numerous but in this case we are able to rule out several. The 1892 and 1893 outbursts of 17P/Holmes were attributed to impacts with a satellite (Whipple 1984) but this possibility is rendered extremely unlikely by a third, similar outburst 115 years later. Rotational breakup requires a rotation period of less than 5.2 hours (assuming a spherical, strengthless body with a density of  $400 \text{ kg m}^{-3}$ ; Richardson & Melosh 2006). Work by Snodgrass et al. (2006), while not revealing a definitive rotation period, suggests a value several times longer. Tidal breakup is implausible given the position of 17P/Holmes (far from any planet or the Sun) at the time of outburst. A possible trigger for the outburst

---

<sup>1</sup>Based on observations obtained with MegaPrime/MegaCam, a joint project of CFHT and CEA/DAPNIA, at the Canada-France-Hawaii Telescope (CFHT) which is operated by the National Research Council (NRC) of Canada, the Institut National des Science de l’Univers of the Centre National de la Recherche Scientifique (CNRS) of France, and the University of Hawaii.

<sup>2</sup>This work is based in part on data products produced at the TERAPIX data center located at the Institut d’Astrophysique de Paris.

is a decrease in the perihelion distance from 2.16 AU to 2.05 AU caused by a close approach to Jupiter in January 2004, resulting in an increase in solar insolation (but only by  $\sim 10\%$ ) to greater depths in the comet’s interior. However, the detailed mechanism by which an increase in insolation might lead to the observed outburst remains unknown.

In this paper we present a set of coordinated observations taken at the Canada-France-Hawaii Telescope (CFHT) in a program designed to monitor the development of the coma in outburst. A major result is the discovery of multiple sub-nuclei ejected from Comet 17P/Holmes during the October 2007 outburst. We discuss their dynamical and physical characteristics and the constraints placed by their existence on the outburst mechanism.

## 2. Observations and Data Reduction

We obtained images in the SDSS  $r'$  filter ( $\lambda_c = 6250 \text{ \AA}$ ) on UT 2007 Nov. 6, 8-15 at the 3.6 m CFHT atop Mauna Kea. The instrument used was MegaCam, a wide-field mosaic camera of 36 CCDs that covers a square-degree field of view (Boulade et al. 2003). Each chip in MegaCam has  $2048 \times 4068$  pixels, with an image scale of  $0''.185 \text{ pixel}^{-1}$ . Two sets of five images were taken on each night using a standard dithering pattern to cover the  $80''$  gaps between chips. The first set had individual exposure times of 50 s and was intended to provide deep imaging of the comet, while the second set had exposure times of 5s to provide unsaturated photometry near the nucleus. Time was allocated through a target-of-opportunity program and images were obtained in queue-scheduled mode. Although non-sidereal tracking was unavailable, trailing losses are not significant in our data as the comet traversed only  $0''.4$  during the 50 s exposures - less than the full-width half maximum, which was typically  $0''.85$ . Pre-processing was done by the Elixir pipeline (Magnier & Cuillandre 2004) which removes the instrumental signature using bias frames and twilight flatfields. For improved astrometric calibration, we resampled the images

using SWarp, released by the Terapix data center at the Institut d’Astrophysique de Paris, and attained  $0''.2$  astrometric accuracy. The dithered images were median-combined using IRAF to produce a contiguous field of view. The weather was seen to be photometric by the CFHT Skyprobe on every night except UT 2007 Nov. 6. Using field stars that could be found in successive images we performed relative photometry across the nine nights of data and found that all nights were consistent to within  $\sim 0.1$  mag. To account for varying levels of extinction between nights we normalized all measurements to those on UT 2007 Nov. 9. Fluxes were converted to calibrated magnitudes using instrumental zero-points calculated by the Elixir pipeline using Landolt fields (Landolt 1992).

Table 1 provides a journal of observations. A sample image (before spatial filtering) is shown in Figure 1 (left panel).

## 2.1. Spatial filtering of images

The very large dynamic range of the coma hinders detection of small embedded features. Therefore, we elected to filter the images to suppress the coma and bring out small-scale fluctuations. Various algorithms to do so exist in the literature (Larson & Slaughter 1992; Schleicher & Farnham 2004), notably the Larson-Sekanina radial and rotational shift-difference algorithm (Larson & Sekanina 1984), which detects asymmetries by subtracting each image pixel from a neighboring pixel separated by offsets  $\Delta R, \Delta\theta$  in nucleus-centered polar coordinates. Different choices of offsets produce sensitivities to various kinds of features. Such a filter has been used on images of 17P/Holmes by Moreno et al. (2008).

We convolved the images with a Laplacian filter (Figure 1), consisting of a positive Gaussian nestled inside a broader negative Gaussian. This type of filter is traditionally

used in image processing as an edge detector, signaling regions where the surface brightness gradient changes. Unlike the Larson–Sekanina filter, this filter is anisotropic and does not assume a center to the coordinate system. The only free parameters are the radii of the two Gaussians. The Laplacian filter is akin to a negative second derivative, and thus produces a positive signal on locally concave portions of the image, like bright trails or fragments. After exploring a range of filter scales, we found an inner Gaussian one- $\sigma$  radius of 3 binned pixels and an outer radius of 6 binned pixels provided greatest sensitivity to the embedded features. A binned pixel is  $1''.85$ . Figure 2 shows the result of applying the Laplacian filter to our images.

For comparison, we also applied the Larson-Sekanina method to our images, with  $\Delta R = 5$  binned pixels ( $9''.25$ ), and  $\Delta\theta = 5^\circ$ . Figure 3 shows the resulting images. A box-car median has been subtracted from the images to improve contrast.

The coma largely vanished in our images when convolved with the Larson-Sekanina algorithm and the Laplacian filter, leaving behind a network of apparent dust trails and possible fragments. While most fragments and dust trails identified in these images can also be identified in those images processed with the Larson-Sekanina filter we find that background objects are better suppressed by the Laplacian filter. To minimize false-detections, we choose to use the Laplace filter on our widefield images of 17P/Holmes.

## 2.2. Detection of fragments

We wrote software to cross-identify persistent brightness maxima in our images. This software displays a Laplacian-filtered image, allows a user to select an apparent fragment, and then scans a  $7 \times 7$  binned pixel region for the brightest  $3 \times 3$  box to find the putative fragment center. We linked candidates from image to image by hand-selecting the same

bright regions found in the previous image. Hence, any motion observed should be genuine, because we allow the peak finding algorithm to hunt for the fragment center. In all, we found 16 fragment candidates, labeled A–P in Figure 2.

### 3. Characterization of the Fragments

#### 3.1. Aperture Photometry

The fragments were originally identified using images processed with a Laplacian filter to highlight small-scale fluctuations. To investigate their photometric properties we used our set of unfiltered long-exposure images.

To minimize background contributions we subtracted the signal from the spherical dust shell surrounding the nucleus. We computed the median of concentric annuli centered on the nucleus, used cubic spline interpolation to calculate a functional form for the coma and subtracted the resulting fit. Using the positions of the detected fragments we centered apertures on 89 locations in the 8 nightly images. The radius of the aperture was varied between  $0''.185$  and  $9''.250$ , corresponding to physical distances of 145 km and 7265 km, respectively. The background coma level was calculated using an annulus with an inner radius of  $11''.1$  and an outer radius of  $14''.8$ . For the following analyses we choose to use an aperture with a radius of  $2''.22$ . Larger apertures tend to introduce large errors from imperfect background subtraction, while smaller apertures fail to include much of the light reflected by the fragments.

### 3.2. Background Comparison

First, we performed aperture photometry on a large sample of background regions to determine if the detected fragments were statistically brighter than the background. These background apertures were centered on a total of 890 points across the 8 images with approximate distances from the nucleus equal to those of the detected fragments and at random position angles.

The resulting distribution of flux from the background apertures is significantly different from the apertures centered on the apparent locations of the fragments (Figure 4). Flux contained within the apertures placed on the background is, on average, zero, as one would expect, given accurate sky subtraction, while those apertures centered on the detected fragments, generally, clearly contain an additional source of light. A Kolmogorov-Smirnov test shows that the probability that the two distributions in the figure are drawn from the same population is  $\ll 10^{-4}$ , meaning that the fragments are inconsistent with noise. We acknowledge that the two distributions overlap slightly. To minimize the impact of false-detections upon the conclusions of this paper, we focus on the ensemble, rather than individual, properties of the fragments.

### 3.3. Spatial Convergence of Fragments

The procedure we have described is, of necessity, subjective. It is difficult to distinguish between a star residual and a tail-less fragment, for example, and it is possible that some of our fragments are simply unconnected random variations in the coma. However, when Figure 2 is viewed as an animation<sup>3</sup> (Figure 1), the expanding nature of the system of fragments is clear.

---

<sup>3</sup>Available for viewing as supplementary online-only material



To verify that the fragments are real, and are not subjectively selected artifacts, we examine the average motion to see whether our fragments converge as expected. For each apparent fragment, we compute a velocity by taking the median of velocities from positions on adjacent nights (Table 2). We also compute a median position across the first three images, giving a snapshot of the entire system at the center time of these images.

We expect any radially expanding system originating at a single time and place to show a linear relationship between velocity and radius. Indeed, Figures 5 and 6 show such a relationship to be present in our data. There is a positive correlation between radius and velocity at the Spearman rank-order probability  $p_{\text{SRO}} = 0.062$ .

We next extrapolate the fragment’s velocity back in time from the fragment’s median position at its median observation time. Figure 7 shows the individual fragments plotted on a single graph, with their motion extrapolated back in time. It is evident that some of the measurements may be spurious or inaccurate, but on average the fragments move radially outward in time.

Finally, we estimate the convergence time of the entire fragment ensemble using the median positions and velocities. Table 3 shows the time and distance of closest approach to the nucleus for each fragment. Figure 8 shows the median distance of the fragments from both the nucleus, and from their common center. For the entire data set, the fragments converge closest to the nucleus at UT Oct  $26.0 \pm 1.0$  and closest to their common center at UT Oct  $25.2 \pm 1.0$ , where the uncertainty is computed through a bootstrapping procedure. This time is within  $2\sigma$  of the likely eruption time of Oct  $23.7 \pm 0.2$  (Wilkening et al. 2007). If we omit fragments *H*, *K*, *N*, and *P*, which fall off the linear relation in Figure 6, then the closest convergence time with respect to both the nucleus and the common center becomes UT Oct  $24.3 \pm 1.2$ , in excellent agreement with Wilkening et al. (2007) and Hsieh et al. (2007), who obtained UT Oct  $23.7 \pm 0.2$  and UT Oct 23.8 (no error given), respectively. We

conclude that the fragments not only radiate outward, but their positions converge at the time of the initial outburst, lending credence to the hypothesis that we are observing pieces of debris from the original outburst.

## 4. Discussion

### 4.1. Phase Space Distribution of Fragments

The position angle of the fragments measured from the nucleus appears uniformly distributed (Figure 7). This suggests that the true three-dimensional distribution is either spherical, or a cone with its axis along the line of sight.

In a radially expanding system, we expect the true and projected positional radii and radial velocities to be perfectly correlated. Comparing both to the same theoretical projected distribution thereby provides an independent validation of the data. An important caveat is that such tests are sensitive to the completeness of the sample. For example, if the manual peak-finding procedure missed slow moving fragments near the nucleus, we may understate the level of central concentration.

In Table 4, we compare the projected distribution of the radii and velocities of the fragments with various three dimensional models. We consider 1) a spherical distribution of fragments; 2) a model in which fragments lie on an infinitely thin shell; 3,4) finitely thick hollow shells (or hollow spheres) of fragments that have 20% and 50% of the thickness of the shell’s radius; 5,6) radially symmetric space-filling distributions of fragments with  $r^{-1}$  and  $r^{-2}$  number density profiles; 7) a line of sight hollow cone of fragments; and 8) a line of sight solid cone of fragments.

For the positions, we use the median radius and time of the first three nights, and for the velocities, we use only the radial component of the best-estimate median velocity,

under the assumption that any transverse component is noise. We consider a set of model distributions consisting of hollow spherical shells of various thicknesses, filled spheres, and filled and hollow cones. We use a Kolmogorov-Smirnov (KS) test to compare our projected  $R$  and  $v$  values with the distribution predicted by each model. This is a slight misuse of the KS test, because we fix our outermost point to be at a cumulative probability of 1. However, our interest is in ruling out models, and this effect will tend to make all models agree better with our data.

Table 4 shows the KS agreement of the distribution of the data with the models. We can rule out the thin shell and the 20% shell (in which the fragments occupy a shell of thickness equal to 20% of the radius) on the basis of both the radial data and the velocity data. The 50% thick shell, solid sphere, and, to a lesser extent,  $r^{-1}$  models are compatible with the data. If the eruption is conical rather than spherical, then an edge-enhanced cone is preferred over one that is solid. In cases in which the radial data disagree with the velocity data, like the 20% spherical shell and the solid cone, we are inclined to believe that the radial data are more robust.

These results must be interpreted taking into account the completeness caveat mentioned above. If we assume that fragments closer than  $0.3 \times R_{\text{max}}$ , where  $R_{\text{max}}$  is the projected radius of the largest fragment, are invisible to us, then the shell-like distributions become less likely, but the centrally concentrated  $r^{-2}$  density model and the solid cone are no longer ruled out. At most, we can claim that the fragment distribution is not concentrated at the peripheries, but we cannot rule out a strongly centralized arrangement. Our conclusion is that the spatial and radial velocity distributions of the fragments in the sky-plane are consistent with isotropic ejection or conical ejection centered around the line of sight, or very close to it.

It is difficult to envisage a plausible scenario in which 16 fragments are ejected

isotropically from the nucleus, without catastrophic disruption of the nucleus. One mechanism has been suggested by Samarasinha (2001) who proposed that small nuclei ( $\sim 1$  km) could contain connected voids that allow sublimated supervolatiles to move rapidly through the nucleus. Assuming these voids have no outlet to the surface, internal gas pressure could build up until it exceeds the tensile strength of the mantle. At this point, an outburst could occur over a large fraction of the nucleus’ surface. A difficulty with this model is the very small tensile strength of the cometary nucleus, which will prevent the build-up of high internal pressures.

## 4.2. Size Estimates

At the earliest detection in our data set, the fragments have magnitudes ranging from  $r' = 17.6$  to  $23.5$  (Table 2). We consider two models to estimate the sizes of the fragments from the magnitudes. The apparent magnitude of a monolithic body is related to the viewing geometry and the body’s physical characteristics according to the relation

$$g_{\lambda}\Phi_{\alpha}C = 2.25 \times 10^{22} R^2 \Delta^2 \pi 10^{0.4(m_{\odot}-m_{\lambda})} \quad (1)$$

where  $g_{\lambda}$  is the geometric albedo,  $\Phi_{\alpha}$  is a function to account for the variation of brightness of the body with phase angle,  $C$  [m<sup>2</sup>] is the geometric cross-section of the body,  $R$  [AU] and  $\Delta$  [AU] are the heliocentric and geocentric distances, and  $m_{\odot}$  and  $m_{\lambda}$  are the apparent magnitudes of the Sun and the body respectively (Jewitt 1991). We use a linear approximation for the phase function and set  $\Phi_{\alpha} = 10^{-0.4\alpha\beta}$ , where  $\alpha$  [deg] is the phase angle and  $\beta$  [mag deg<sup>-1</sup>] is the phase-coefficient. We assume a value of 0.035 mag deg<sup>-1</sup> for the phase-coefficient (Lamy et al. 2004) and  $m_{\odot} = -26.95$  mag when using the SDSS  $r'$  filter (Ivezić et al. 2001).

Model A: If the detected fragments are monolithic, spherical bodies with geometric albedos of 0.1, we infer that the median radius of a fragment is 1.79 km, with sizes ranging from 0.8 km to 3.0 km (Table 2). Since the radius of the parent nucleus is only  $\sim 1.7$  km (Lamy et al. 2000; Snodgrass et al. 2006) this interpretation can be rejected. Increasing the albedo to 0.15 yields a range of radii from 0.6 km to 2.4 km with the median radius being  $\sim 1.5$  km. We conclude that it is unlikely that the fragments are bare nuclei, and instead proceed to consider the possibility that they are actively-outgassing sub-nuclei.

Model B: Using the complementary set of 5 second exposures obtained on the same nights at CFHT, we measured the brightness of the unsaturated nucleus, without coma-subtraction. We find that the apparent magnitude corresponds to an effective radius of  $\sim 330$  km, demonstrating that the dust coma around the nucleus dominates the scattering cross-section, as it appears to do for the fragments we have discovered. Thus, the magnitude of the fragment ( $m_f$ ) or nucleus ( $m_n$ ) depends primarily on the amount of dust present in the aperture. Assuming that the nucleus and the fragments have material sublimating from active regions that cover similar fractions of their surfaces, then the difference of the observed magnitudes is proportional to the ratio of their surface areas, or their radii squared if we assume spherical bodies:

$$10^{-0.4(m_f - m_n)} = \frac{R_f^2}{R_n^2} \quad (2)$$

where  $R_f$  and  $R_n$  are the radii of the fragment and the nucleus, respectively. Using this scaling argument, and apparent magnitudes of the fragments and nucleus determined using  $2''.22$  circular apertures as described in Section 3.1, we obtain fragment radii between 10 m and 110 m on the first night of detection (Table 2). Cometary nuclei typically have active regions that cover only a small percentage of the surface (A’Hearn et al. 1995; Jewitt 2004), due to the gradual formation of an inert mantle by irradiation, micro-meteorite

bombardment and loss of volatiles. It is possible that the fragments were more active than the nucleus. They may have been rotating rapidly and exposing much of their surface to sunlight, or composed mainly of volatile material with little or no mantle. Thus, the sizes derived here should be considered as upper limits.

With a density of  $400 \text{ kg m}^{-3}$  (Richardson & Melosh) and the scaled radii listed in Table 2 for Model B we find that the sixteen fragments have a combined mass of  $10^{10} \text{ kg}$ , corresponding to  $\sim 0.1 \%$  of the mass of a  $1.7 \text{ km}$  radius, spherical nucleus. Again, this is an upper limit to the mass in the fragments, and shows that the outburst of 17P/Holmes ejected only a tiny fraction of the total nucleus mass.

### 4.3. Acceleration

We do not detect any systematic acceleration of the fragments between 2007 Nov. 6 and 2007 Nov. 14 UT, since a single mean velocity over the observational dataset predicts a time of ejection that agrees with the published eruption time (Wilkening et al. 2007). This suggests two things: firstly, that radiation pressure does not significantly affect the motion of the fragments and, secondly, that the fragments are not self-propelled by directional sublimation of volatiles. The first point suggests that the fragments are macroscopic, as opposed to clusters of micron-sized particles, or smaller, that would be easily accelerated in the anti-solar direction by radiation pressure. The second constrains the nature of the fragments. Given that these fragments are volatile-rich and actively outgassing (as demonstrated in §4.2), one may expect self-propulsion to accelerate the fragments in the anti-solar direction, as volatiles would be typically expelled in the sunward-direction. However, the fragments are likely to be spinning rapidly and may be isothermal, resulting in sublimation in all directions, and hence no net acceleration. Thus, the fragments are observed to continue in the directions in which they were ejected, with no noticeable

increase in velocity.

#### 4.4. Correlation of Flux with Radius

If the observed surface brightness maxima originate from discrete solid fragments expelled by gas pressure, we expect lighter fragments to be launched faster, and so to appear at larger radii. Specifically, if we make the assumption that the observed fragments are icy fragments of size  $\ell_f$ , density  $\rho_f$  and mass  $m_f = \rho_f \ell_f^3$ , and are ejected by gas pressure  $P$  acting over a fixed acceleration distance  $d$ , then the energy transmitted to each fragment is  $\frac{1}{2}m_f v_f^2 = P \ell_f^2 d$ , and each fragment’s distance to the nucleus  $r_f$  is given by  $r_f \propto v_f \propto \ell_f^{-1/2}$ , where  $v_f$  is the fragment’s velocity. Assuming that a fragment’s brightness is given by its (sublimating) surface area  $\ell_f^2$ , the expected relationship of  $r_f$  to photon flux  $f_f$  is then  $r_f \propto f_f^{-1/4}$ .

Alternatively, if we change our assumptions so that the gas pressure acts for a fixed time  $t$  instead of a fixed distance  $d$ , then the imparted momentum is  $P \ell_f^2 t = m_f v_f$ , and  $r_f \propto f_f^{-1/2}$ . In both instances, fragment brightness should be weakly anti-correlated with non-projected radius  $r$ . In a two dimensional projection onto the sky radius  $R$ , the above inverse relation will be somewhat washed out. Nevertheless, we still expect to find brighter fragments at smaller radii.

Figure 9 shows the observed relationship of sky radius,  $R$ , to flux. There is a statistically significant (Spearman rank-order  $p_{\text{SRO}} = 0.017$ ) positive correlation between  $R$  and flux, in contrast to the expected anti-correlation. It is reassuring that a strong deficit of faint fragments at small  $R$  was not observed, because this would be suggestive of a selection bias against finding fragments in the bright central coma near the nucleus. The fact that the shape of the flux distribution varies with  $R$  is consistent with the space-filling

distribution suggested by §4.1, because a thin expanding shell of fragments would produce a distribution of fluxes that is invariant in  $R$ .

In conclusion, the observation that flux increases rather than decreases with radius argues against a model in which the fragments consist of monolithic fragments with a sublimation rate and reflective flux proportional to their surface area. Otherwise, by simple gas pressure arguments, one would expect the largest and heaviest fragments to be closest to the nucleus. Instead, each detected fragment might in fact be a collection of active objects, rather than a single cohesive fragment.

#### 4.5. Fragment Fading

Figure 10 shows the temporal fading of the nucleus and the median of the fragments’ magnitudes during our observations. The nucleus fades at a rate of  $0.15 \text{ mag day}^{-1}$  while the fragments, on average, fade at a similar rate of  $0.19 \text{ mag day}^{-1}$ . Figure 11 rescales the flux of each fragment to a common baseline using an exponential fit with a shared time constant. Over the nine days plotted, the fragments fade by about 80%.

We checked the functional form of the fade and find that an exponential fit is best, but that linear and quadratic fits cannot be ruled out. We evaluate the significance of differences among the linear, quadratic, and exponential models by bootstrap resampling the data set. We resample from the set of fragments themselves, to create simulated data containing the same number of fragments, but with possible repeats of individual fragments’ time series. In 5000 resamplings, the quadratic model is favored over the linear model in 99.1% of instances; the exponential model is favored over the linear model in 98.6% of instances; and the exponential model is favored over the quadratic model in 97.9% of instances. We conclude, with  $\gtrsim 2\sigma$  certainty, that the fading of the fragments is best described by an



exponential law, or a constant fractional fading per unit time. In Figure 11 we plotted the best exponential falloff rate of  $0.18 \text{ day}^{-1}$ , representing a 5.6 day exponential time scale.

We solved the sublimation equilibrium equation for icy grains with Bond albedo 0.1 to find maximum sublimation rates of  $\sim 5 \times 10^{-8} \text{ m s}^{-1}$  (for a flat slab perpendicular to sunlight) to  $\sim 10^{-9} \text{ m s}^{-1}$  (for an isothermal sphere). Using these sublimation rates and the exponential time scale of 5.6 days, we calculate fragment sizes of  $5 \times 10^{-4} \text{ m}$  to  $0.02 \text{ m}$ . These sizes are much too small to account for the observed magnitudes of the fragments, unless each fragment observed is in fact a collection of icy grains.

In Appendix A, we show that a power law distribution of sub-fragments sublimating at a constant rate naturally produces an exponential decay in emission, as is observed.

## 5. Physical processes of ejection

The relative velocities of the fragments are puzzlingly high. Typically fragments ejected from short-period comets have separation velocities of a few meters per second (comparable to the nucleus escape velocities; Boehnhardt 2004) but our measurements show typical velocities of  $\sim 100 \text{ m s}^{-1}$  on the sky-plane. We note that observations of split comets are usually performed weeks or months after the event, at which time high-speed fragments that are fading, like those considered here, would no longer be detectable. Thus, the deficit of small, active, high-velocity fragments around other split comets may be due to observational biases, and the nature of the material ejected during the 2007 outburst of 17P/Holmes may not be particularly unusual. However, the mechanism responsible for accelerating these fragments to velocities of  $\sim 100 \text{ m s}^{-1}$  is difficult to establish. We consider several possibilities.

Could rotational fragmentation account for the measured velocities? The shortest

possible rotation period for 17P/Holmes is 5.2 hours. If the nucleus rotates faster than this then it will break up, assuming it is a strengthless body. This rotation period corresponds to a surface velocity of just  $0.6 \text{ m s}^{-1}$ , ruling out rotational disintegration as mechanism of expulsion.

We also consider the possibility that the fragments were expelled slowly, and then accelerated like rockets by the reaction against their own sublimation. The first problem with this “rocket” model is that acceleration would be in the anti-solar direction, meaning that the true velocity must be four times greater than the largest  $\sim 100 \text{ m s}^{-1}$  spatial velocity observed, because the line of sight is nearly parallel to the motion, and only a small component of the velocity appears as tangential motion on the sky. Thus, there is no way to account for the  $\sim 100 \text{ m s}^{-1}$  transverse velocities observed when the transverse motion is not aligned with the projection of the anti-solar direction.

Moreover, it is difficult to account for the absolute speed of the fragments using rocket propulsion. The rocket equation gives, for a rocket of initial mass  $m_i$ , final mass  $m_f$ , and exhaust velocity  $v_e$ , a rocket velocity  $v_r = v_e \ln(m_i/m_f)$ . For a non-rotating sublimating fragment, however, the exhaust is emitted over a hemisphere, rather than through a rocket nozzle, so that half the momentum is lost, and  $v_r = v_e \ln(m_i/m_f)/2$ . Assuming that the exhaust velocity is given by the  $(3/2)k_B T$  energy of water molecule at a 190 K sublimation temperature, and allowing no loss of energy into the water molecules’ rotational modes,  $v_e = 511 \text{ m s}^{-1}$ . To achieve a final velocity of  $400 \text{ m s}^{-1}$ , 84% of the fragments’ mass must be sublimated as rocket fuel, implying that their radius decreases by half during acceleration. At the fastest plausible sublimation rate of  $5 \times 10^{-8} \text{ m s}^{-1}$ , taken to occur over a ten day acceleration period, this fraction implies a maximum initial fragment radius of 0.08 m. However, the thermalization time of a fragment of ice of this size is about half a day, so that the fragments would quickly become isothermal and the asymmetrical sublimation

that provides the propulsion would cease long before the necessary velocity was reached.

So, the measured ejection velocities are difficult to explain. The most plausible ejection method is through gas pressure. In the simplest possible model, a pressure  $P$  ejects a mass of linear size  $L$ , acting over a distance of  $L$  before the gas dissipates. Such a process would resemble an explosion occurring under the fragments. If one assumes porous fragments with a density  $\rho = 400 \text{ kg m}^{-3}$ , the pressure required is given by equating work done,  $PL^2L$ , with kinetic energy,  $\rho L^3 v^2/2$ , giving  $P = \rho v^2/2 \sim 2 \times 10^6 \text{ Pa}$ . It is possible for CO gas to create such a pressure.

It has been hypothesized that a runaway crystallization of amorphous ice may provide enough energy to cause CO ice to sublime, but this scenario presents many problems in the context of 17P/Holmes. If this is a surface explosion, then the explosive reaction must propagate through the medium at approximately the fragment velocity of  $100 \text{ m s}^{-1}$ , in order for the gas to push the fragments before it dissipates. However, the transition heats the ice only by less than 40 K. For the transition to propagate at explosive speeds, the reaction time  $\tau$  must be under a millisecond, given a propagation speed of  $\sqrt{\kappa/\tau}$ , where  $\kappa \sim 3 \times 10^{-7} \text{ m}^2 \text{ s}^{-1}$  is an upper bound for the thermal diffusivity of ice. However, it is difficult to heat the ice from a highly stable state where  $\tau$  is days or weeks, to a state in which it is so unstable that  $\tau < 3 \times 10^{-11}$ , using only the energy of the transition.

It may be possible to mitigate some of these difficulties by postulating that the acceleration distance is much larger than the fragment size. For example, there may be a broad gas emitting region of size  $h$  on 17P/Holmes, creating a flux of gas normal to the surface, so that fragments would feel a push for a larger distance  $\sim h$  from the surface. The pressures required would then be reduced to  $P \sim \rho(L/h)v^2/2$ . This might reduce the amount of gas flux required, but may not remove the need for a fast propagating reaction.

Alternatively, we could suppose that fragments are accelerated along an extended

trajectory, as in a vent. In this case, we would expect the following equation of energy conservation to hold, neglecting friction and gravity:

$$\frac{1}{2}v^2 = \int_{P_i}^{P_f} \frac{dP}{\rho} \quad (3)$$

If the fluid is a mixture of gas and solid, with gas fraction  $f$  by weight, then the overall density is

$$\rho = \left( \frac{f}{\rho_{\text{gas}}} + \frac{1-f}{\rho_{\text{solid}}} \right)^{-1} \quad (4)$$

Assuming that the solids dominate, and act as a thermal reservoir that keeps the expansion isothermal at temperature  $T$ ,  $P = \rho_{\text{gas}} R_g T$ , where  $R_g$  is the universal gas constant. Then the final fluid velocity is given by

$$\frac{1}{2}v^2 = \frac{1-f}{\rho_{\text{solid}}} (P_i - P_f) + f R_g T \ln(P_i/P_f) \quad (5)$$

If one assumes that the pressure arises from a conversion of mass fraction  $f = 0.1$  CO, that  $\rho_{\text{solid}} = 400 \text{ kg m}^{-3}$ , and that the pressure falls to 1/3 of its initial value when the fluid reaches the surface, then the final velocity is  $70 \text{ m s}^{-1}$  for  $f = 0.10$ , and  $23 \text{ m s}^{-1}$  for  $f = 0.01$ . Changing the pressure at the surface affects the final velocity only modestly. It appears that a 10% CO fraction could provide just enough gas production for the velocities observed, assuming eruption from a vent.

## 6. Summary

We have identified and characterized fragments that were ejected from the nucleus of 17P/Holmes during its spectacular outburst in October 2007. Our findings are as follows:

1. Sixteen fragments are detected in Laplacian-filtered images where the coma has been suppressed using an azimuthal average.

2. The motion of the fragments implies either isotropic or conical ejection from the nucleus on UT 2007 Oct.  $24.3 \pm 1.2$ .
3. Results from aperture photometry are inconsistent with inert, monolithic bodies. Modeling the fragments as sublimating cometesimals yields radii of 10 m to 110 m. Assuming a density of  $400 \text{ kg m}^{-3}$ , the fragments account for  $10^{10} \text{ kg}$  of the total mass ejected, or  $\sim 0.1 \%$  of the nucleus mass.
4. The fragments move unusually fast, with on-sky velocities of up to  $125 \text{ m s}^{-1}$ . Acceleration by CO (or other supervolatile) gas drag forces might be able to generate such large velocities given appropriate launch conditions at the nucleus.
5. We detect no systematic acceleration of the fragments and deduce that the bodies are not self-propelled by sublimation in a preferred direction.
6. The fragments fade at a rate of  $\sim 0.19 \text{ mag day}^{-1}$ , consistent with the idea that they are active bodies, eventually becoming inert as surface volatiles are depleted.

The authors thank CFHT Director Christian Veillet for allocating time to this target of opportunity program and Pierre Martin, Jean-Charles Cuillandre, and the QSO team at CFHT for providing observational assistance. Pedro Lacerda and Bin Yang provided helpful comments. We appreciate support from a NASA Outer Planets Research grant to DJ.

## 7. References

- A’Hearn, M. F., Millis, R. L., Schleicher, D. G., Osip, D. J., Birch, P. V. 1995, *Icarus*, 118, 223
- Boehnhardt, H. 2004, in *Comets II*, ed. M. C. Festou et al. (Tucson: Univ. Arizona Press), 301
- Boulade, O., et al. 2003, *Proc. SPIE*, 4841, 72
- Buzzi, L., Muler, G., Kidger, M., Henriquez Santana, J. A., Naves, R., Campas, M., Kugel, F., Rinner, C. 2007, *IAU Circ.* 8886
- Dohnanyi, J. S. 1969, *J. Geophys. Res.*, 74, 2531
- Hsieh, H. H., Fitzsimmons, A., Pollacco, D. L. 2007, *IAU Circ.* 8897
- Holmes, E. 1892, *The Observatory*, 15, 441
- Ivezić, Z. et al. 2001, *AJ*, 122, 2749
- Jewitt, D. C. 1991, in *Comets in the Post-Halley Era*, 1, 19
- Jewitt, D. C. 2004, in *Comets II*, ed. M. C. Festou et al. (Tucson: Univ. Arizona Press), 659
- Lamy, P. L., Toth, I., Fernández, Y. R., Weaver, H. A. 2004, in *Comets II*, ed. M. C. Festou et al. (Tucson: Univ. Arizona Press), 223
- Lamy, P. L., Toth, I., Weaver, H. A., Delahodde, C., Jorda, L., A’Hearn, M. F. 2000, *BAAS*, 32, 1061
- Landolt, A.U. 1992, *AJ*, 104, 340
- Larson, S.M., Sekanina, Z. 1984, *AJ*, 89, 571

- Larson, S. M., Slaughter, C.D. 1992, Proc. ACM, 337
- Magnier, E. A., Cuillandre, J.-C. 2004, PASP, 116, 449
- Moreno, F., Ortiz, J. L., Santos-Sanz, P., Morales, N., Vidal-Núñez, M. J., Lara, L. M., Gutiérrez, P. J. 2008, ApJL, 677, L63
- Palisa, F. 1893, Astron. Nachr, 132, 31
- Richardson, J. E., Melosh, H. J. 2006, Abstract 1836, Lunar and Planetary Science Meeting XXXVII
- Samarasinha, N. H. 2001, Icarus, 154, 540
- Schleicher, D.G. 2009, AJ, 138, 1062
- Schleicher, D.G., Farnham, T.L. 2004, in *Comets II*, ed. M. C. Festou et al. (Tucson: Univ. Arizona Press), 449
- Snodgrass, C., Lowry, S. C., Fitzsimmons, A.. 2006, MNRAS, 373, 1590
- Whipple, F. L. 1984, Icarus, 60, 522
- Wilkening, L. L., Sherrod, P. C., Sekanina, Z. 2007, CBET, 1118

Table 1. Journal of Observations

UT Date	Telescope	Camera	Filters	$r_H$ [AU] <sup>1</sup>	$\Delta$ [AU] <sup>2</sup>	$\phi$ [deg] <sup>3</sup>	Image scale [km/pixel]
2007 Nov 6.4	CFHT	MegaCam	r'	2.49	1.62	13.7	218
2007 Nov 8.5	CFHT	MegaCam	r'	2.50	1.62	13.3	218
2007 Nov 9.5	CFHT	MegaCam	r'	2.50	1.62	13.1	218
2007 Nov 10.5	CFHT	MegaCam	r'	2.50	1.62	12.9	218
2007 Nov 11.5	CFHT	MegaCam	r'	2.51	1.62	12.7	218
2007 Nov 12.5	CFHT	MegaCam	r'	2.51	1.62	12.5	219
2007 Nov 13.5	CFHT	MegaCam	r'	2.52	1.63	12.3	219
2007 Nov 14.5	CFHT	MegaCam	r'	2.52	1.63	12.2	219
2007 Nov 15.5	CFHT	MegaCam	r'	2.52	1.63	12.0	219

<sup>1</sup>Heliocentric distance

<sup>2</sup>Geocentric distance

<sup>3</sup>Phase Angle



Table 2. Fragment Characteristics

Fragment	Magnitude <sup>1</sup>	Radius [m]		Velocity <sup>2</sup> [m s <sup>-1</sup> ]
		Model A <sup>3</sup>	Model B <sup>4</sup>	
A	19.9	1009	37	104 ± 55
B	19.5	1234	45	65 ± 37
C	23.5	194	10	56 ± 2
D	18.6	1850	68	35 ± 1
E	18.3	2101	77	80 ± 12
F	18.7	1785	66	48 ± 33
G	20.4	820	30	44 ± 62
H	18.3	2149	79	55 ± 34
I	18.8	1690	62	108 ± 48
J	18.8	1678	62	112 ± 78
K	17.7	2853	105	123 ± 24
L	17.6	2942	108	110 ± 68
M	17.6	2991	110	91 ± 36
N	18.9	1618	60	125 ± 53
O	18.5	1895	70	88 ± 146
P	20.4	791	29	102 ± 68

<sup>1</sup>Determined using an aperture of radius 2''.22 and from the image in which the fragment was first detected.

<sup>2</sup>Velocity errors are obtained by resampling from the set of pairwise day-to-day velocities, and computing the 68% limit of the absolute deviation from the un-resampled median.

<sup>3</sup>Radius calculated assuming a geometric albedo of 0.1.

<sup>4</sup>Radius calculated assuming activity similar to that of the nucleus.

Table 3. Date of Closest Approach to Nucleus

Fragment	UT of Closest Approach	Distance of Closest Approach ["]
A	2007-10-27.2	14.8
B	2007-10-22.5	20.1
C	2007-10-22.9	15.6
D	2007-10-23.2	28.1
E	2007-10-22.7	16.6
F	2007-10-20.6	3.1
G	2007-10-22.0	27.8
H	2007-10-05.7	44.3
I	2007-10-24.7	37.8
J	2007-10-22.1	5.3
K	2007-10-29.9	15.5
L	2007-10-26.1	0.6
M	2007-10-24.4	16.2
N	2007-10-31.8	19.1
O	2007-10-25.7	13.6
P	2007-11-01.4	31.4

Table 4. Models of the Spatial Distribution of Fragments

Fragment Distribution	Radial $p_{\text{KS}}$	Velocity $p_{\text{KS}}$
Filled sphere	0.54	0.31
Thin spherical shell	0.0017	0.12
20% spherical shell	0.022	0.59
50% spherical shell	0.84	0.45
$r^{-1}$ density	0.10	0.071
$r^{-2}$ density	0.00029	0.003
Thin cone	0.25	0.98
Solid cone	0.05	0.016
Mixed thin and solid cone	0.38	0.33

Note. — Statistical agreement (Kolmogorov-Smirnov  $p$ ) of various model fragment distributions with the distribution of the fragments on the sky. The models are described in §4.1.

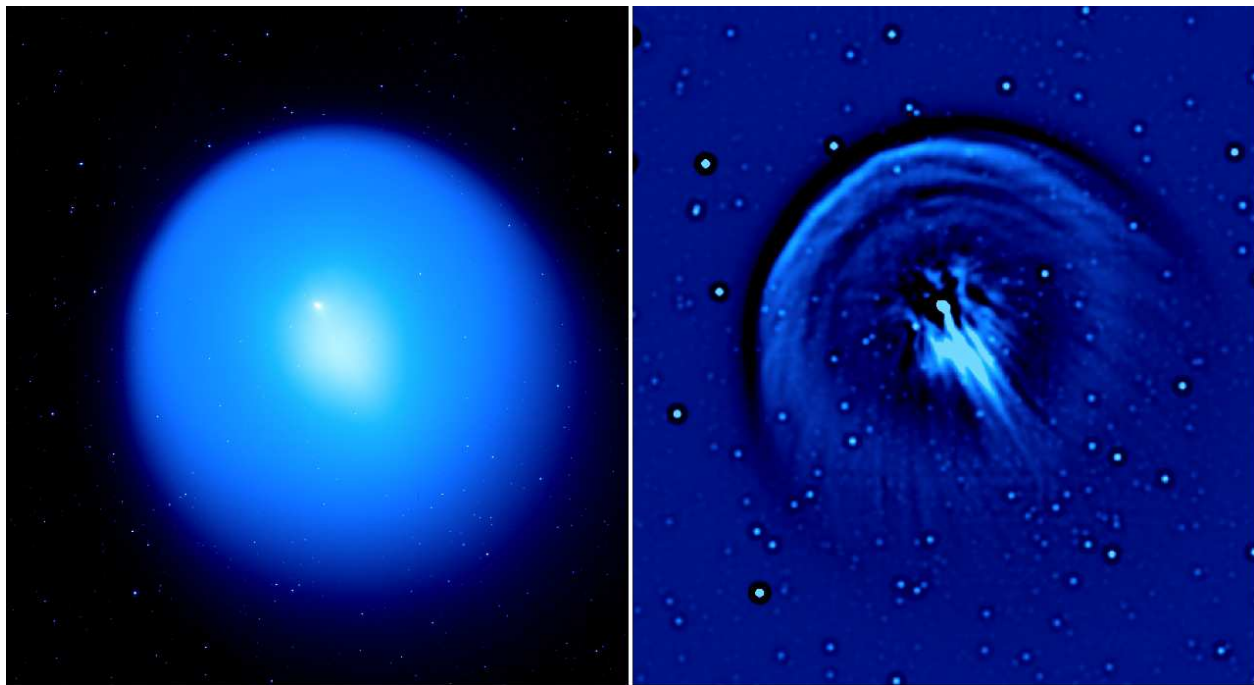


Fig. 1.— Both images are  $25.2' \times 27.6'$ , with north up and east to the left. Left: A 50 second exposure of 17P/Holmes on UT 2007 Nov. 6. The nucleus can be seen north of the center but most morphological features are hidden by the almost-spherical dust shell surrounding it. Right: The same 50 second exposure after convolution with a Laplacian filter. Small-scale features, including dust streaks, background stars, and fragments, are revealed.

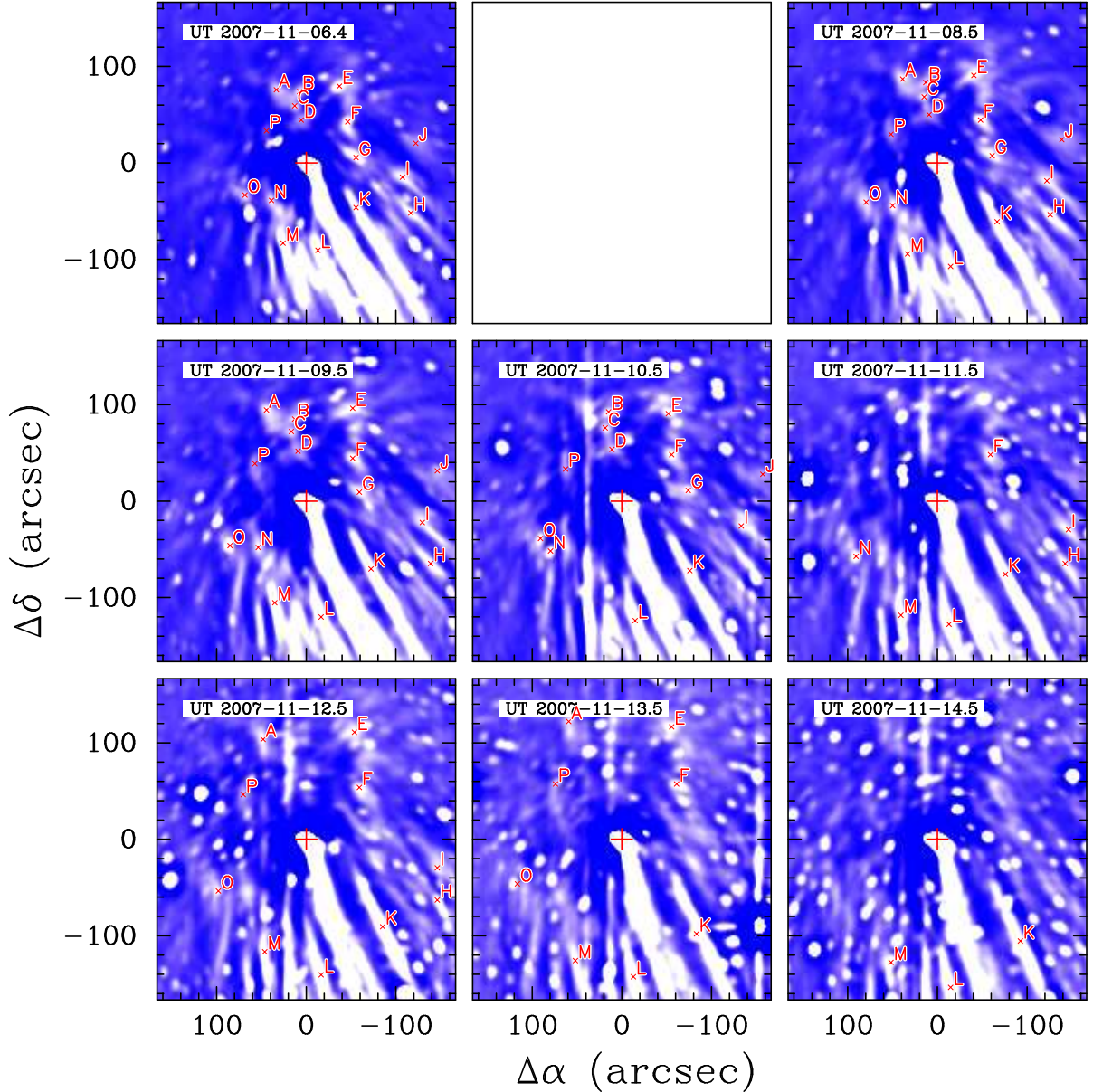


Fig. 2.— Laplacian-filtered images of Comet Holmes in the usual North up, East left coordinate system. There is one image per night, except that no observations were obtained on the second night. The plus symbol indicates the fitted position of the nucleus, and the  $\times$  symbols, labeled A–P, are the fragment positions found through an interactive fitting procedure. Some of the fragments appear to be in the middle of extended tails, but with contrast adjustment they do in fact look like brighter spots. Many of the fragments vanish with time, leaving only three in the final image above. Most of the features in the image are star residuals, and the vertical streaks are remnants of the chip edges from the combining of mosaic images. The last night had no detections, and is omitted.

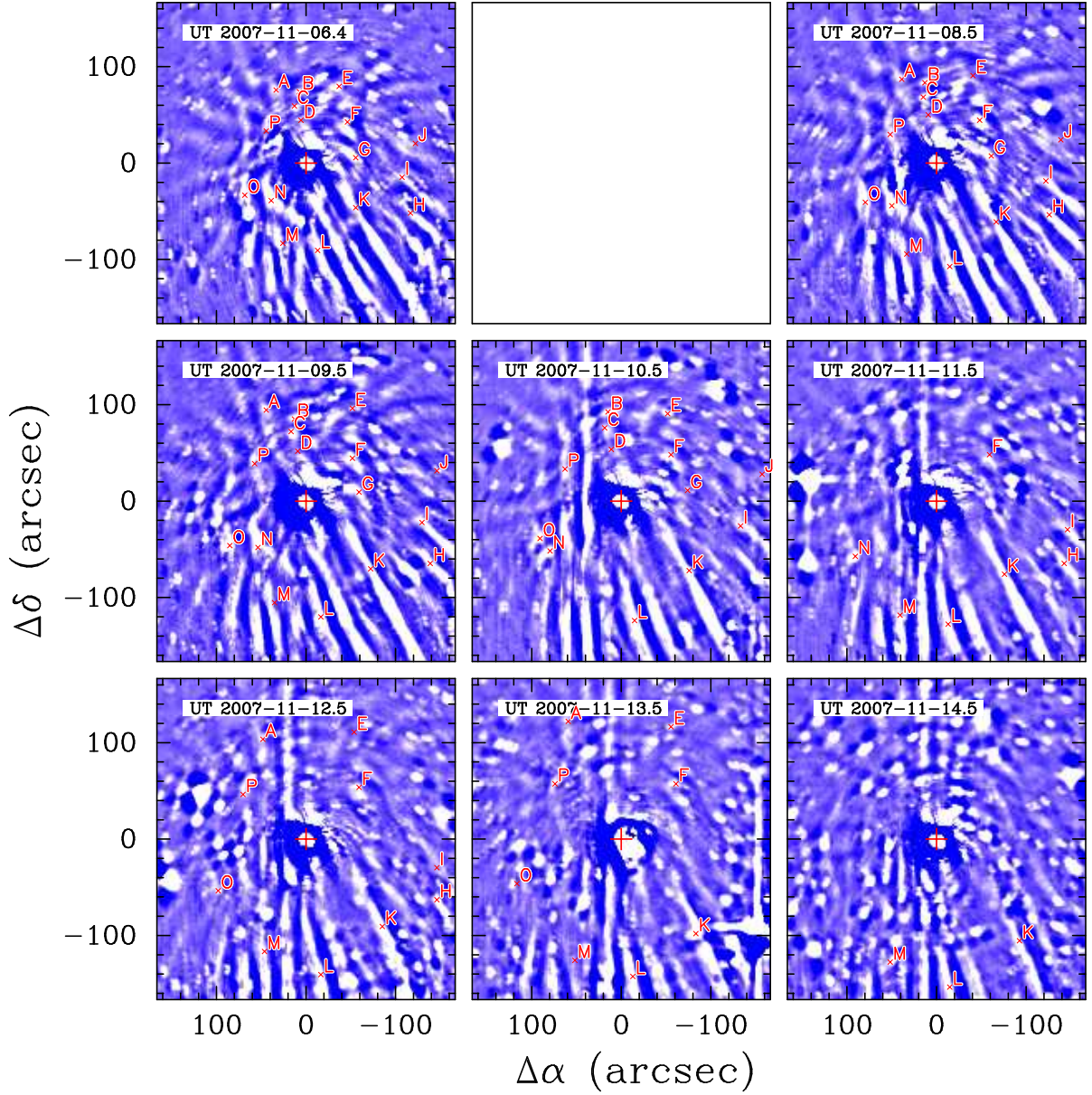


Fig. 3.— Images of 17P/Holmes that have been processed with the Larson-Sekanina method in the usual North up, East left coordinate system. There is one image per night, except that no observations were obtained on the second night. Background objects, such as stars, are obvious throughout the images, and interfere with attempts to identify potential fragments around the nucleus. For this reason, we choose to use Laplacian-filtered images, as shown in Figure 2.



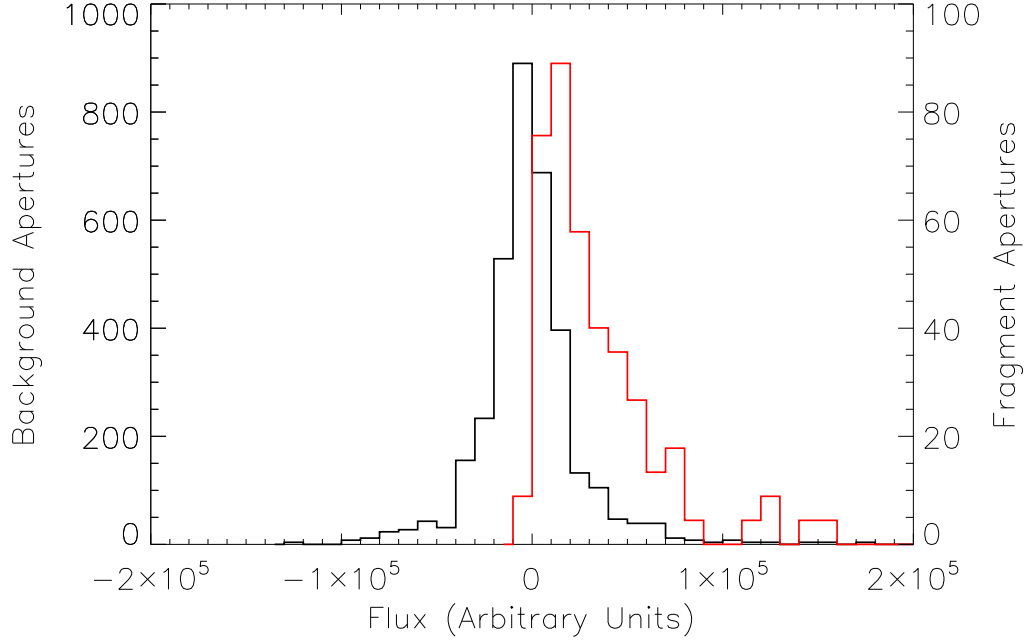


Fig. 4.— Comparison of fluxes contained within 890  $2''.22$  radius apertures placed on the background (black line, left y-axis) and 89  $2''.22$  radius apertures centered on the fragments detected in the Laplacian-filtered images (red line, right y-axis). Both samples are normalized for the sake of clarity. The fragments are systematically brighter than the background. The two samples shown in the histogram have a probability of being drawn from the same population of  $\ll 10^{-4}$ . Fluxes of some fragments fall slightly below zero due to the uncertainties introduced by sky subtraction.

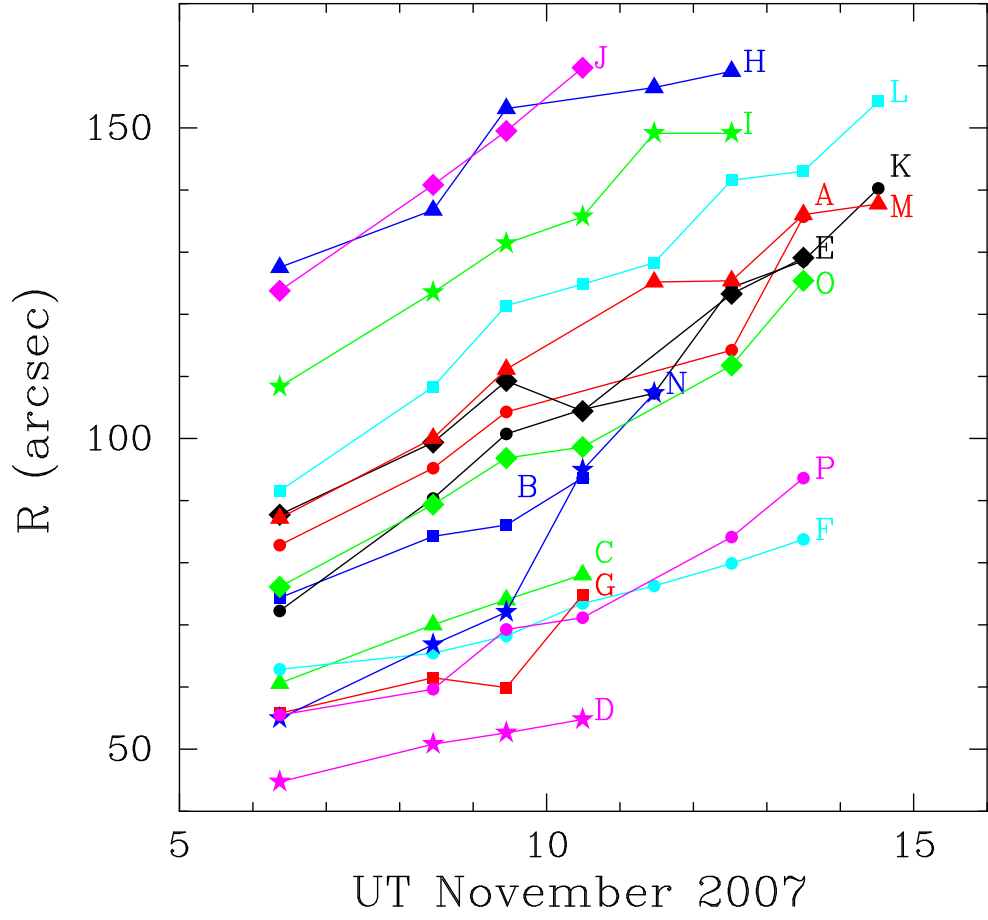


Fig. 5.— The projected distance  $R$  between each fragment and the nucleus, as a function of time.



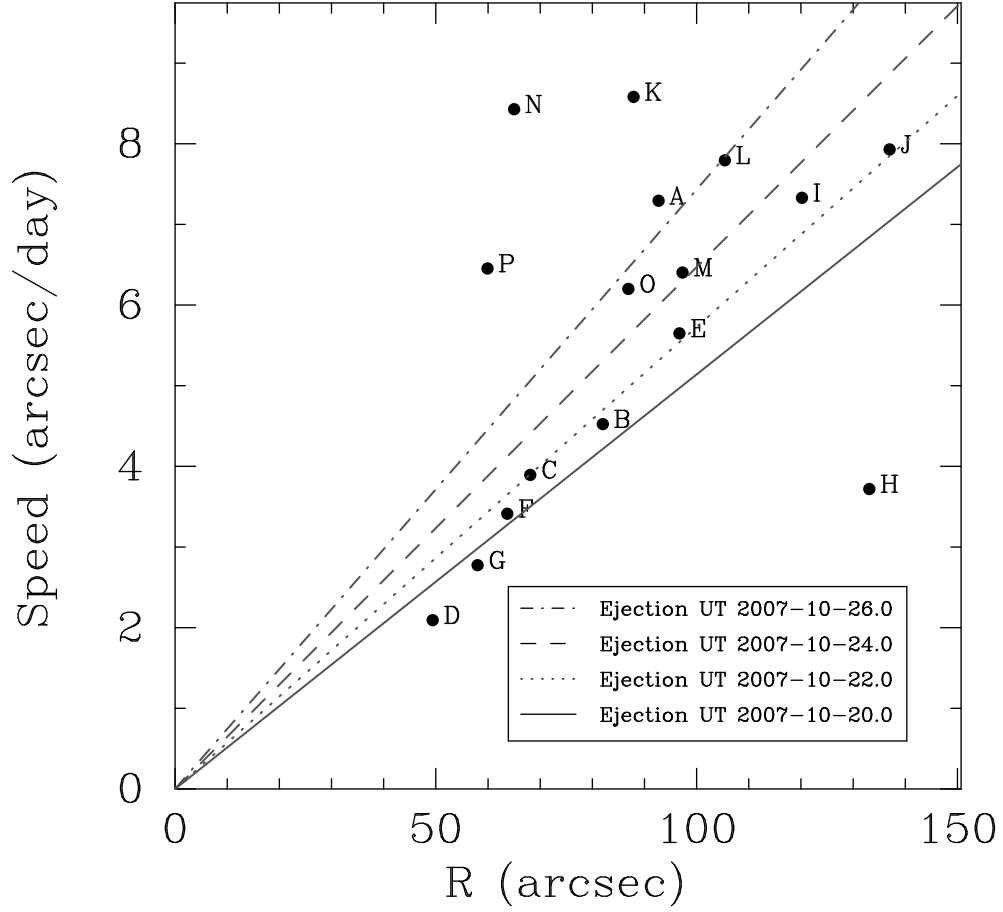


Fig. 6.— The velocity versus radial position of the fragments plotted in Figure 2, with the lines representing the velocity–radius relationship that causes convergence at a particular date. The relationship between velocity and  $r$  is statistically significant at the  $p = 0.06$  level according to Spearman’s  $r$  test.

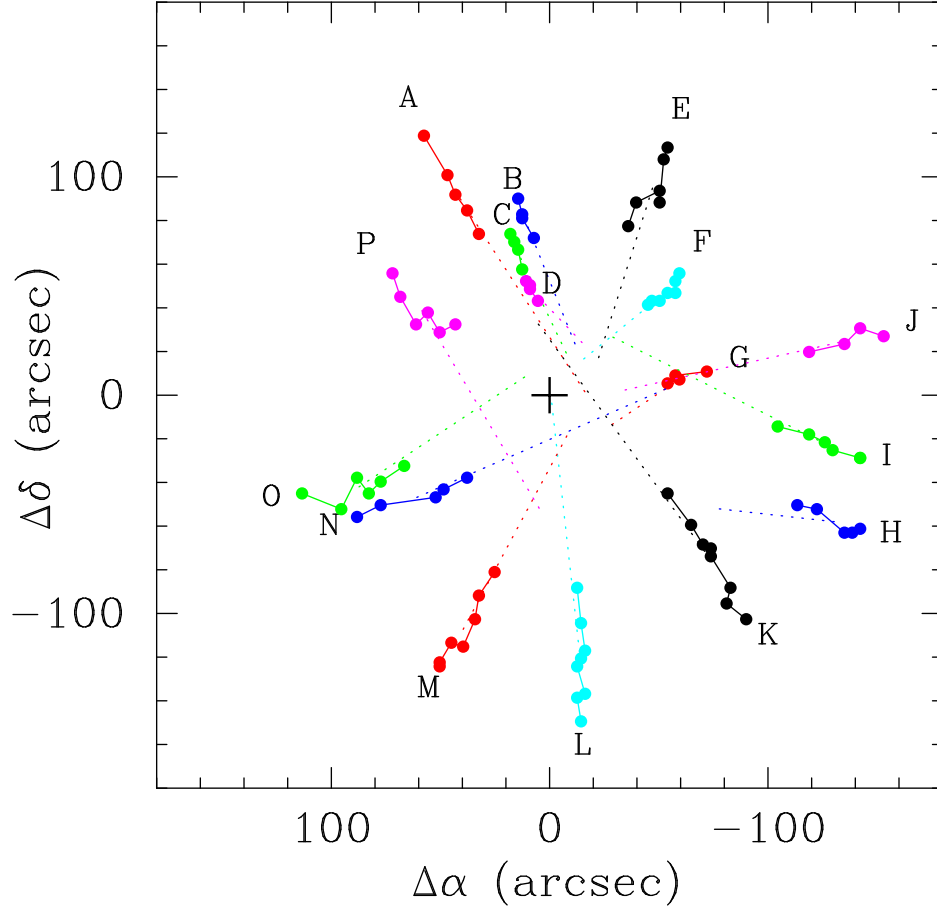


Fig. 7.— The positions of the fragments in Figure 2, with dotted lines representing the extrapolation of each fragment back in time, based on the fragment’s median velocity and position. Although the individual positions are noisy, the ensemble of fragments converges close to the nucleus.

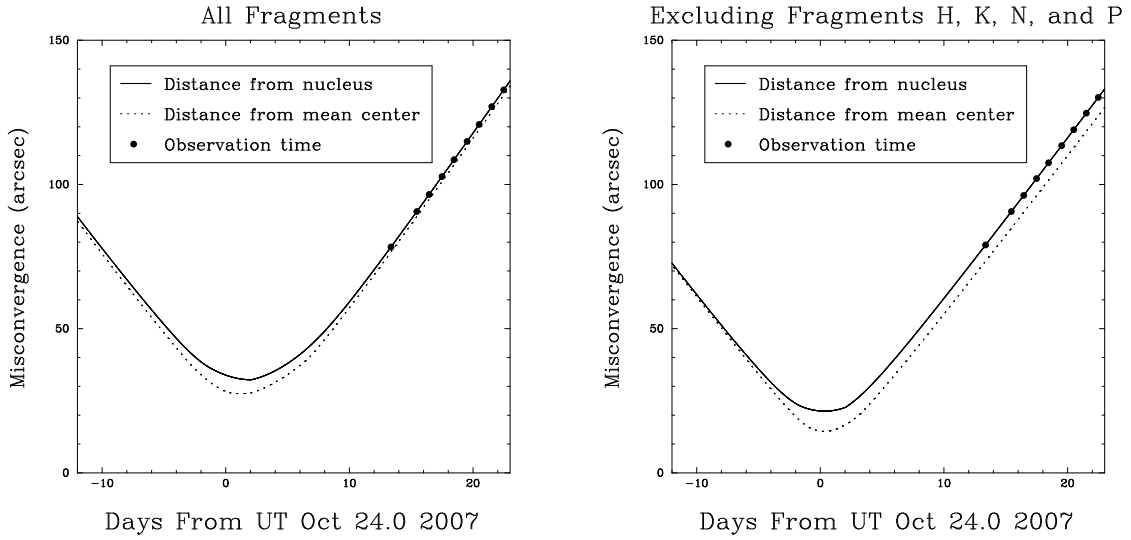


Fig. 8.— The mean distance of the fragments from the nucleus and from their mean center, extrapolated backward in time. Points indicate days on which we obtained observations. The left panel uses all the fragments, and the right panel excludes potential outlier fragments  $H$ ,  $K$ ,  $N$ , and  $P$  as identified from Figure 6. The times of convergence are in  $2\sigma$  ( $0.5\sigma$ ) agreement with published estimates of the outburst date for the complete (truncated) data sets.

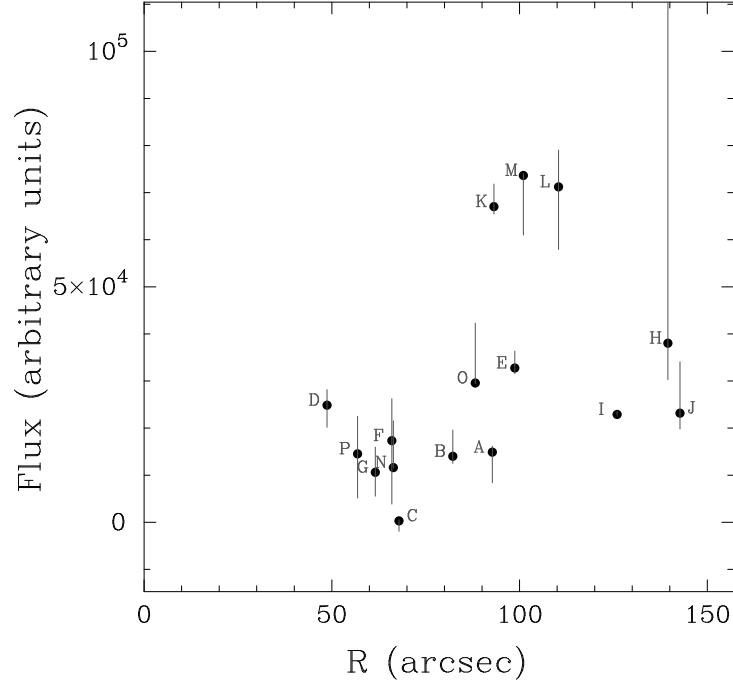


Fig. 9.— Relationship of the projected radial distance from the nucleus,  $R$ , to each fragment’s median photometric flux, both quantities averaged over the first three nights after accounting for fading. The vertical bars span the minimum and maximum of the three nightly fluxes for each fragment. There is a statistically significant positive Spearman correlation ( $p = 0.017$ ) between  $R$  and flux, the opposite of what one would expect if smaller fragments were expelled at a higher velocity.

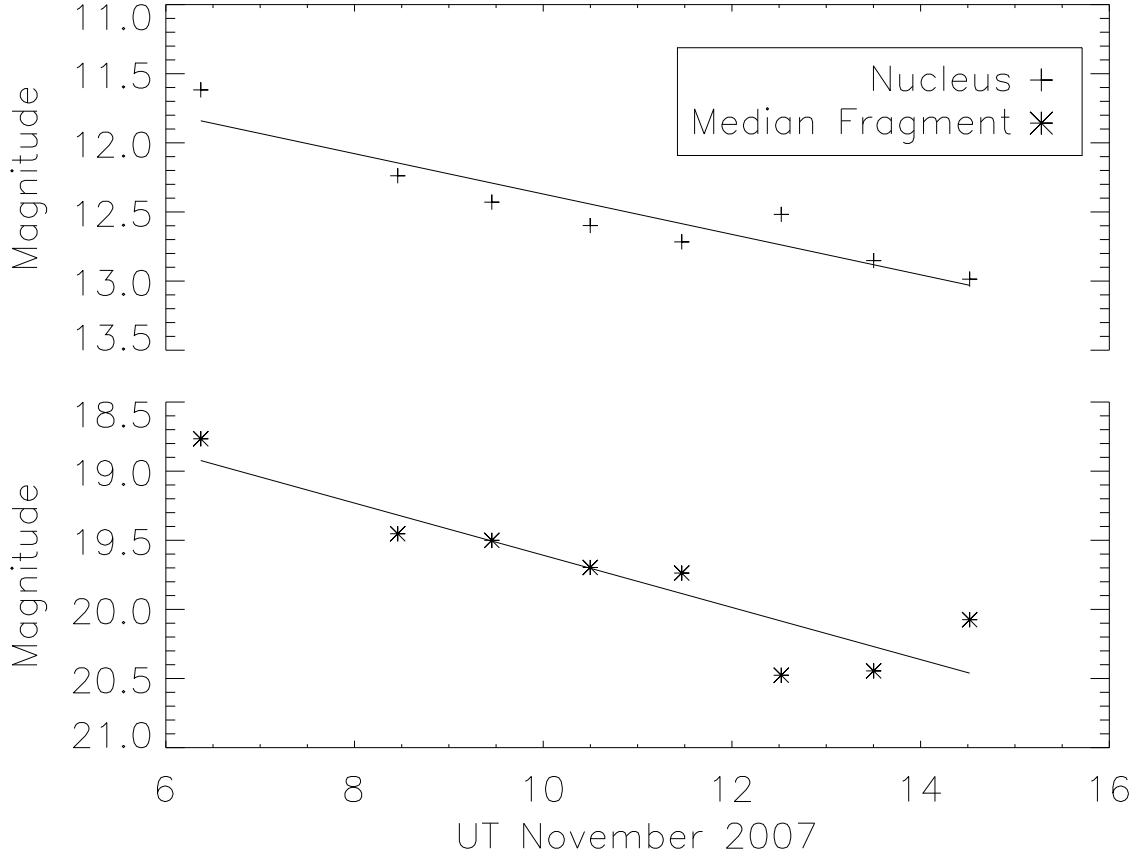


Fig. 10.— Magnitudes of the nucleus and the median fragments as determined from  $2.22''$  aperture photometry. Linear fits to each line yield fading rates of  $0.15 \text{ mag day}^{-1}$  and  $0.19 \text{ mag day}^{-1}$  for the nucleus and average fragment respectively.

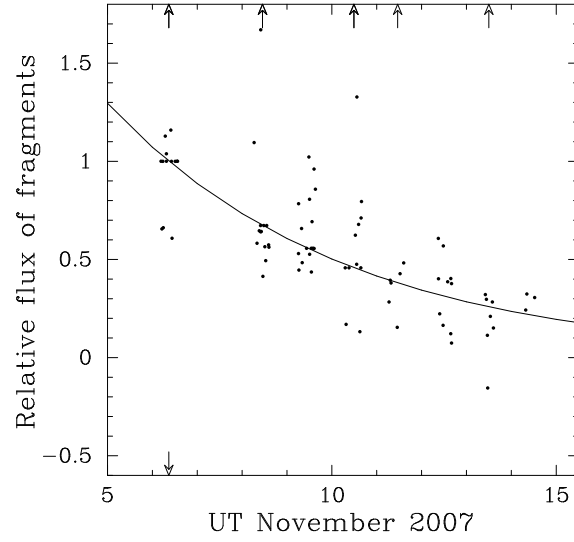


Fig. 11.— Fading of the fragments with time. Based on the best exponential fit of the entire data set, the flux of each fragment at each measured time was rescaled so that the fits of all fragments have a flux of 1.0 on the first night, and then plotted as a point. The solid curve is the best-fitting exponential  $\exp(-0.18 \times \text{time})$ , where time is in days. Arrows indicate outliers falling off the plot. For the purpose of plotting only, the x-axis values have been randomized slightly to prevent points from overlapping.

### A. Constant fractional fading per unit time: a swarm of particles?

As noted above, there are several problems with a model consisting of monolithic sublimating fragments of material whose brightness scales as the surface area. The brightest (largest) fragments are not the closest to the nucleus, the least bright fragments do not fade notably faster, and the best fit fading law is exponential rather than quadratic in time.

Accordingly, we consider “fragments” that are in fact swarms of particles obeying a power law distribution instead of single large fragments. Such a power law distribution arises naturally in collisional fragmentation or grinding processes (Dohnanyi 1969). If the fragments are actually a distribution of small particles rather than monolithic pieces, their brightness, fading rate, and radial distribution are no longer expected to be coupled, which is what we observe.

We assume that each fragment consists of a differential distribution of sub-fragments of size  $\ell_f$ :

$$N(\ell_f) \propto \ell_f^{-\alpha} \quad \text{for} \quad \ell_f \in [\ell_{f1}, \ell_{f2}] \quad (\text{A1})$$

Taking a constant sublimation rate  $\dot{\ell}_f < 0$  summed over the combined area of the sub-fragments, this distribution produces an observed flux:

$$F(t, \alpha, \ell_{f1}, \ell_{f2}) \propto \int_{\max(\ell_{f1} - \dot{\ell}_f t, 0)}^{\max(\ell_{f2} - \dot{\ell}_f t, 0)} \ell_f^2 (\ell_f - \dot{\ell}_f t)^{-\alpha} d\ell_f \quad (\text{A2})$$

$\dot{F}(t)/F(t)$  is readily shown to be inversely proportional to  $t_v = \ell_{f2}/\dot{\ell}$ , the timescale of the vanishing of the largest fragment  $\ell_{f2}$ . In Figure 12, we consider several values of the exponent  $\alpha$ , and for each value we fix value of  $t_v$  that gives  $d/dt \ln F(t) = -0.18$  at  $t=15.5$ , like the real data. We find that for all  $\alpha$  considered,  $\dot{F}(t)/F(t)$  is constant over the

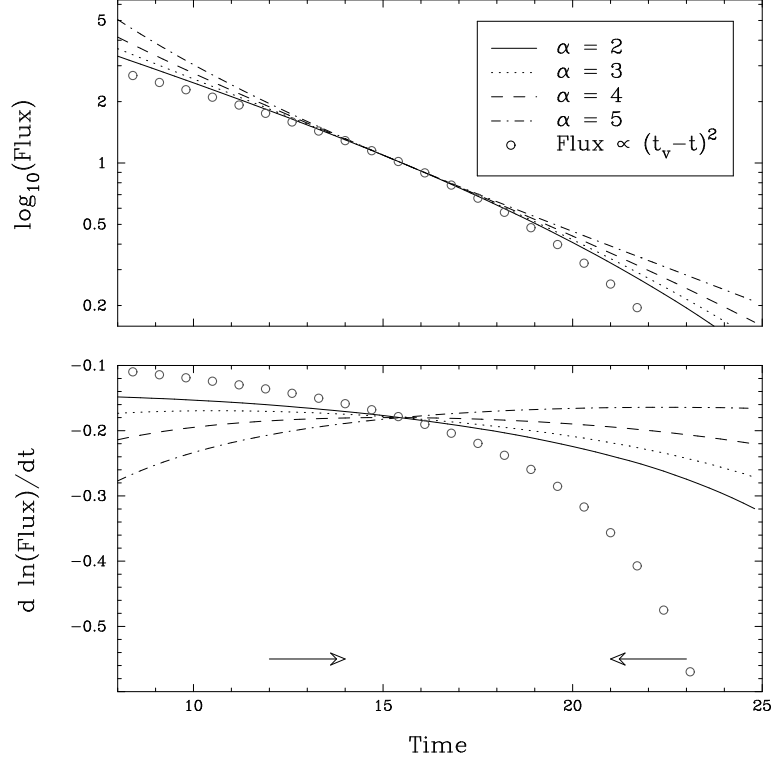


Fig. 12.— The fragment flux and its logarithmic derivative as a function of time, assuming that each fragment actually consists of a  $\ell_f^{-\alpha}$  differential distribution of particles, and that each particle has a flux proportional to its area  $\ell_f^2$ , as described in equations A1 to A2. At each  $\alpha$ , we adjust the one free parameter so that  $\dot{F}/F = 0.2$  at  $t = 15.5$ , as seen in Figure 9. It is evident that all of the exponents  $\alpha$  produce an approximately exponential decay curve during the observation timespan, denoted by the the arrows. In contrast, a single-fragment model ( $\circ$  symbols) with  $F(t) \propto (t_v - t)^2$  produces an accelerating falloff during the span of observations.



observational window, in agreement with our fit of the actual fading.

We conclude that fragments are plausibly explained as clusters of sub-fragments, obeying a power law distribution, with the power law index anywhere between  $-2$  and  $-4$ . Such a model is consistent with the observed constant logarithmic fading rate, and allows the fading rate, fragment brightness, and distance from the nucleus to be independent, as observed.